Channelised, distributed, and disconnected: subglacial drainage under a valley glacier in the Yukon Supplementary material

Camilo Rada and Christian Schoof

Department of Earth, Ocean and Atmospheric Sciences, University of British Columbia. 2207 Main Mall, Vancouver, BC Canada.

Correspondence: Camilo Rada (camilo@rada.cl)

1 Data quality

The analysis of the pressure records from South Glacier presented in this paper does not rely on the accuracy of absolute pressure values, in the sense that we have not attempted to use the differences in water pressures between different boreholes as an indication of hydraulic potential gradients. If a sensor is incorrectly calibrated and, for instance, the amplitude of recorded diurnal pressure oscillations is miscalculated, our interpretation of connection between boreholes would be unaltered in sections 3.2 and 3.4 of the main paper. Unless the calibration coefficients are wildly incorrect, variations in the amplitude of diurnal oscillation over longer periods of time will still resemble each other even if the computed pressure difference between the boreholes varies spuriously. However, we do rely on the calibration parameters being stable over time. Otherwise, inferred variations in the amplitude of diurnal oscillations would be affected by calibration drift, and would not necessarily represent the changes in the drainage response to surface forcing. Similarly, we rely on calibration coefficients being stable in order to infer whether isolated boreholes experience a seasonal drift in water pressure during summer in section 3.1.

There are numerous mechanisms by which a sensor can become corrupted. An obvious cause is signal cable damage, which is sometimes visible at the glacier surface due to crevasse opening. We have visually identified records that show signs of such corruption, such as large, random jumps in pressure between successive measurements, and large negative water pressures.

Transient high-pressure spikes (Kavanaugh and Clarke, 2000) are likely to have caused abrupt calibration changes in four of the recorded pressure time series. From 2013 onwards, most sensors were equipped with snubbers, and only one sensor displayed this issue afterwards. In all four cases, instantaneous offsets were manually identified and corrected.

Eleven boreholes were equipped with two sensors, logged independently. These sensors recorded in total more than 13 years of duplicated data. Seven of the boreholes included a digital transducer, in which the measurement is made in the sensor, while the remaining sensors were analogue sensors, which rely on voltage measurements at the surface and can, therefore, be corrupted by damage to the signal cable introducing partial short circuits. Assuming that the two sensors in these boreholes remain hydraulically connected, their records allow us to assess data quality and calibration drift.

All presented pressure values were computed from differential voltage readings using a linear transformation of the form

$$P = MV - P_0, \tag{1}$$

where P is the pressure at the sensor and V the ratio of a measured differential voltage to an applied excitation voltage on a Wheatstone bridge circuit, one of whose limbs is a strain gauge bonded to the pressure sensor diaphragm. The calibration constants are the offset P_0 (corresponding to the voltage measured at atmospheric pressure), and the multiplier M. Our reported measurements rely on pre-installation calibrations and assume no change in calibration constants.

Panel a of each of Figs. 1–11 shows the pressure at one sensor in a given borehole, computed using pre-deployment calibration values of M and P_0, plotted against the corresponding value for the other sensor in the same borehole, for all doubly-instrumented boreholes. If both sensors record the same pressure, then these phase plots should lie along the black dotted line $P_2 = P_1$, as the expected hydrostatic pres-

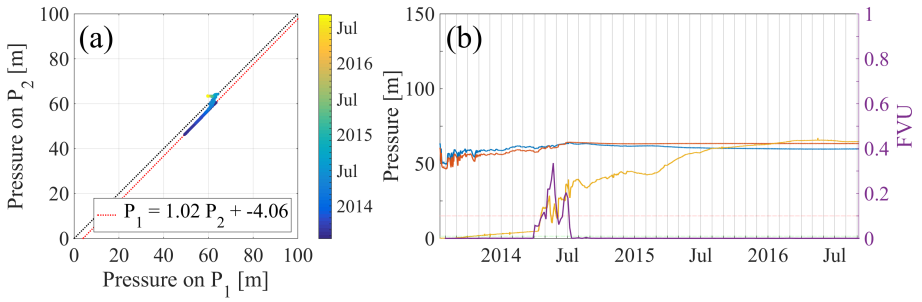

Figure 1. Pressure records P_1 and P_2 for the two sensors in borehole 13H16, installed 20 cm apart. (a) A phase plot with points colour-coded by time. The expected relationship $P_1 = P_2$ is shown as a black dotted line. The linear regression model constructed over the first month after installation is shown as a red dotted line, with parameter values given in inset box. (b) Pressure time series for P_1 (blue) and P_2 (orange). The residual between P_2 and the linear regression model is shown in yellow, scaled by a factor of 10 for visibility. Unexplained variance over a one-month moving window is shown as a purple line.

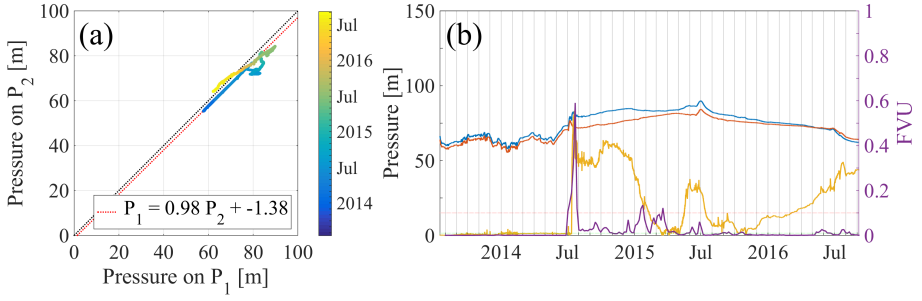

Figure 2. Pressure records for the two sensors in borehole 13H17, installed 34 cm apart, plotted using the same scheme as in Fig. 1

sure difference between the two sensors is minimal (except perhaps in figure 3). Given that there could be small errors in the calibration parameters, we estimate a transformation between P_1 and P_2 with a linear regression over the data recorded during the first month after installation (red dotted line). Deviations from that line indicate that one or both of the sensors are not behaving linearly as in equation 1, the calibration constants have changed, or that the two sensors have become isolated from each other due to freezing or ice creep.

In panel b of each figure, the pressure recorded at each sensor as computed from pre-installation calibration is presented as a blue or orange line. Also plotted is the difference between the recorded pressures. This difference is calculated after applying the linear regression model correction computed over the first month of sensor operation (indicated in the inset in panel a). This residual has been multiplied by a factor of 10 for easier visibility and plotted as a yellow line.

To quantify changes in the similarity of both records, we have also computed linear regressions over moving one-month windows, and subsequently calculated the fraction of unexplained variance (FUV) over that period. The FUV is the fraction of the variance in P_2 that cannot be explained by variations in P_1. As such, it is a measure of the quality of a linear fit: if samples are taken at times $t_1, t_2, ..., t_N$ the FUV would be

$$FUV = \frac{\sum_{i=1}^{N} (P_1(i) - P_2'(i))^2}{\sum_{i=1}^{N} (P_1(i) - \mu_1)^2} \tag{2}$$

where $P_1(i)$ is the value of P_1 at time t_i, $P_2'(i)$ is the value of P_2 at time t_i, transformed linearly using regression model over the moving one-month window. N is the number of samples in the window and μ_1 is the mean of P_1.

We see that except for Fig. 4, all differences in pressure are smaller than 5 meters, and deviations in the multiplier (the difference between the coefficient of P_1 in the formula in panel a and the expected value of one) are in most cases smaller than 2%. In figures 4 and 7, where anomalously large slopes are observed, we can see that there is a clear change in the slope below a certain pressure, suggesting that the sensors used most likely did not behave linearly over their nominal calibration pressure range. A similar effect probably affects the sensors in Fig. 5, where the two sensors may have also become disconnected from each other. In all cases, the non-linearity seems to occur only in the digital sensors, and these make up a small fraction of the whole dateset.

In the first month of each time series, the residual remains below 5 meters and the FUV below 1%. Such consistent records can extend for more than one year (Fig. 7), but the agreement between the sensors can also degrade after a few

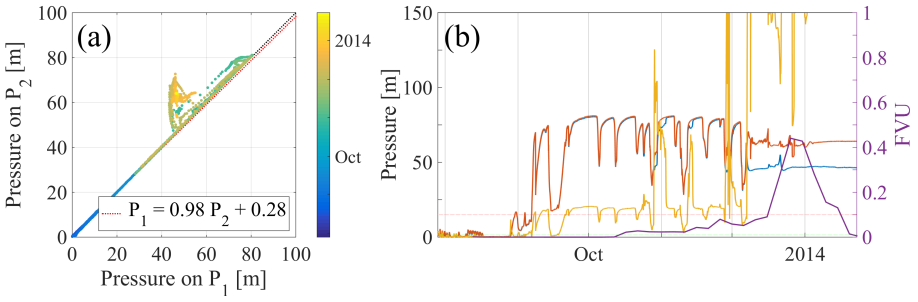

Figure 3. Pressure records for the two sensors in borehole 13H58 (the "fast-flow" borehole of the main paper), installed 70 cm apart, plotted using the same scheme as in Fig. 1.

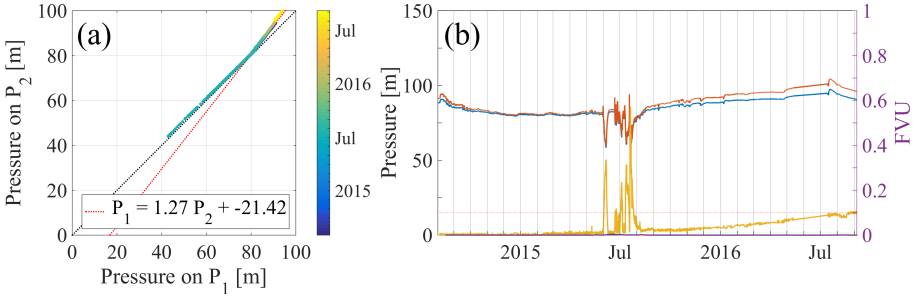

Figure 4. Pressure records for the two sensors in borehole 14H60, installed 20 cm apart. P_2 was recorded by a digital sensor. The plotting scheme used is the same as in Fig. 1.

months. The increase in the residual usually starts at a very specific point in time. This is suggestive of a loss of the connection between the two sensors. Some examples of possible disconnection are evident in Fig. 2 in July 2014, in Fig. 3 in December 2013, Fig. 6 in late July 2015, and Fig. 9 in October 2015. It is unlikely that the difference observed in these cases arise from a single, transient high-pressure spike changing the calibration of the sensor instantly: the pressure records should then still be linearly related to each other, but with different offsets and multipliers, and the FUV should remain small.

A few records (for instance those in Figs. 1 and 5) are consistent with a gradual change in the offset and/or multiplier. However, this effect seems to be small in comparison with the differences arising from possible disconnection.

Disconnection can be explained by sensors becoming encased in ice due to ice creep or due to freezing, the latter being less likely if we consider that radar measurements indicate the presence of temperate ice at the base. The fact that with most disconnections happen after the end of the summer season, and happen sooner in sensor pairs that are consistently recording low water pressures (for instance Fig. 6), is consistent with disconnection by creep closure; the ice surrounding the corresponding boreholes should be subject to higher creep rates. It is important to note that residuals and FUV are typically very small over periods where diurnal variations are present, and that significant inconsistencies between sensor pairs in the same borehole appear in the absence of such variations, indicating a loss of connection to the drainage system.

Doubly instrumented boreholes also allow us to assess the effect of pressure snubbers on pressure records. In figures 3, 4, and 7 to 11, sensor P1 (blue) was equipped with a snubber and P2 (orange) was not. In figures 1 and 2, both sensors had snubbers, and in figures 5 and 6 neither of them did. In the cases where only one sensor had a snubber, it can be seen that no smoothing of the pressure signal is observed. Close examination of the pressure time series shows that even spikes lasting a few minutes are well-reproduced by both records. Therefore, at the sampling frequencies of our sensors (1 to 20 minutes), the effects of the snubber are negligible. By contrast, among the sensors not equipped with a snubber, one out of 48 suffered large, "instantaneous" pressure offsets, contrasting with only one in 174 experiencing the same among sensors equipped with a snubber. Therefore, pressure snubbers seem to be effective at filtering out the transient high-pressure spikes ("fluid hammer") that are thought to be responsible for those offsets through damaging the sensor diaphragm, but without affecting the accuracy of the instruments for measuring slower pressure variations.

Tests of the sensors extracted by re-drilling after one year also found that small offsets had developed, in all cases smaller than 3 m. Multiplier changes were also observed, but they account for an even smaller error within the mea-

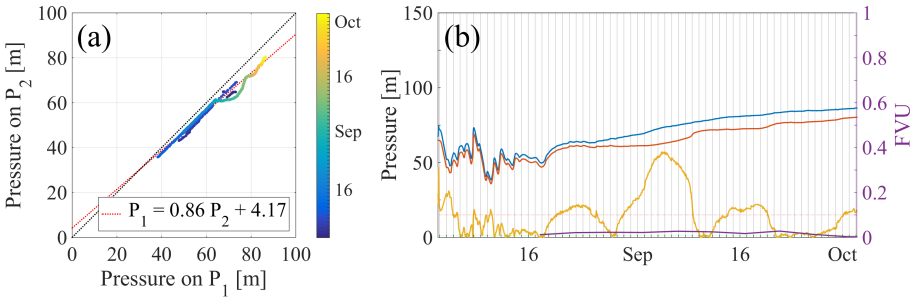

Figure 5. Pressure records for the two sensors in borehole 14H62, installed at the same elevation. P_2 was recorded by a digital sensor. The plotting scheme used is the same as in Fig. 1.

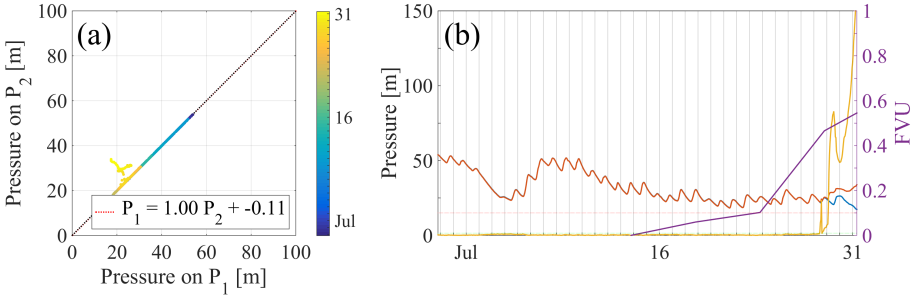

Figure 6. Pressure records for the two sensors in borehole 15HL07, installed at the same elevation. The plotting scheme used is the same as in Fig. 1.

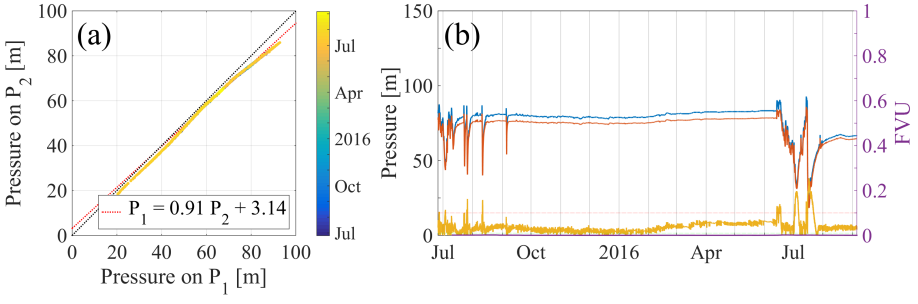

Figure 7. Pressure records for the two sensors in borehole 15HU01, installed at the same elevation. P_2 was recorded by a digital sensor. The plotting scheme used is the same as in Fig. 1.

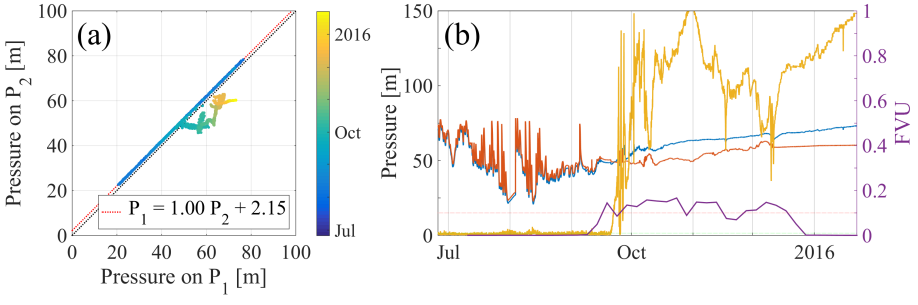

Figure 8. Pressure records for the two sensors in borehole 15HU04, installed at the same elevation. P_2 was recorded by a digital sensor. The plotting scheme used is the same as in Fig. 1.

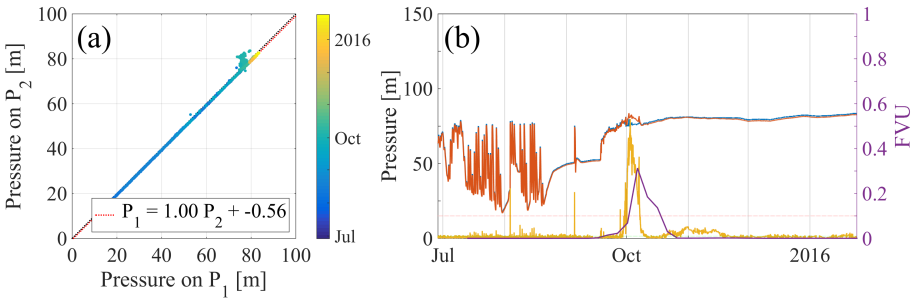

Figure 9. Pressure records for the two sensors in borehole 15HU05, installed at the same elevation. P_2 was recorded by a digital sensor. The plotting scheme used is the same as in Fig. 1.

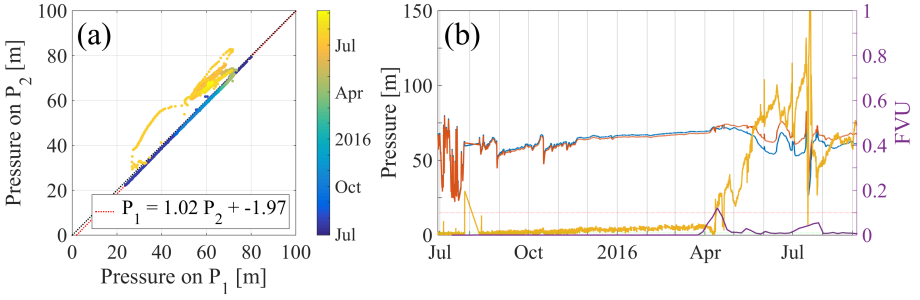

Figure 10. Pressure records for the two sensors in borehole 15HU17, installed at the same elevation. P_2 was recorded by a digital sensor. The plotting scheme used is the same as in Fig. 1.

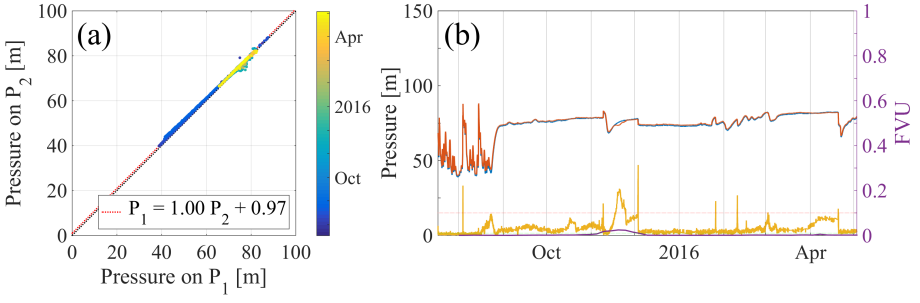

Figure 11. Pressure records for the two sensors in borehole 15HU50, installed at the same elevation. P_2 was recorded by a digital sensor. The plotting scheme used is the same as in Fig. 1.

sured pressure range. The observation of a few records in the dataset gradually drifting up to nearly 200% of overburden is therefore difficult to explain and we were not able to correct for it. The effect may be due to errors in initial calibration or hard-to-diagnose sensor damage, or due to calibration drift that is sufficiently rare or extreme not to have been captured by the relative small sample of sensors in doubly-instrumented or re-drilled boreholes. One possible cause of large calibration errors developing could be the permanent deformation of the sensing diaphragm by ice formation against it.

Instrumental accuracy and precision aside, our interpretation relies on water pressures having been measured at the bed, except in cases where the sensor is known to have been installed englacially (such as hole A in Fig. 2). Recall that sensors were typically installed 10-20 cm above the bed; we are relying on the connection to the bed not becoming closed off. We observe that sensors in doubly-instrumented boreholes can start to exhibit independent pressure variations during winter, sometimes reverting to a common signal. One example can be seen in the two sensors displayed in Fig. 3 and Fig. 13 of the main text, both installed 70 cm apart in the same hole (the fast-flow borehole). One possible explanation for the mismatched data could be the sensors becoming encased in ice during the winter and thus separated from each other.

There is direct evidence for processes that could lead to sensors becoming enclosed in ice, for example, the digital confinement data shown in Fig. 15 of the main text (see section 4.4 of the main text). Note that the fraction of boreholes

showing diurnal variation in their second summer season decreases compared with the first, dropping from 71% in the first season to 58% in the second. This drop in activity could also be a consequence of sensors becoming encased in ice or otherwise isolated from the bed.

2 Reliability of temperature as a melt proxy

In section 3.4 of the main text, we use the standard deviation of the temperature over a 1-day running window as a measure of diurnal variations in meltwater input. That variation is then used to compute the curve in Fig. 12c, showing the ratio of the amplitude of pressure variations in the connected part of the subglacial drainage to variations in meltwater input. Later, in section 4 of the main text, we attribute the increase in the relative amplitude to an increase in the efficiency of the drainage system. However, it could be argued that the same signal can arise from changes in the degree-day factor through the season. To address this question, we present an assessment of the variability of degree-day factors and a calculation of the relative amplitudes using an independent proxy of melt variability.

To assess the variability of the degree-day factor, we used melt output of the energy balance model described by Wheler and Flowers (2011), covering the years 2007-2009 and 2011-2012. For each day, we computed the degree-day factor that would explain the modelled melt from that day's PDD value. Fig. 12 shows the results during four different summer seasons (2009 was excluded due to the existence of many outliers in the melt record). It can be observed that after an initial increase, the degree-day factors are fairly stable in some years (2007 and 2012), while in others (2008 and 2011) they can have significant variations, with the monthly running mean changing by a factor up to 2.5. Such variations would however be insufficient to explain the signal of Fig. 12c, in where the relative amplitude increases by a factor of 4.2.

As we have no melt model results for 2015, we cannot however directly rule out larger variations in the degree-day factors for that year. Nevertheless, large variations in the degree-day factor are less likely in the period between July 4th and 30th where there were no snowfall events, or significant changes in the relative extent of old snow and bare ice evident in the time-lapse images. During the same period, the relative amplitude shown in Fig. 12c increased by a factor of 1.6, a variation unlikely to be explained by a degree-day factor change.

We also re-computed the relative amplitude of Fig. 12c of the main text over a shorter period (until August 27th) for which surface elevation changes were measured by a sonic ranger SR50 at the AWS location (see Fig. 2 in the main text). In this alternative approach, we used surface lowering as a proxy for melt amplitude instead of the standard deviation of the positive part of temperature. The caveat of this approach is that again we cannot measure melt rate in mass of water per unit time directly, but now have to account for density variations between between fresh snow, old snow and ice. In the model by Wheler and Flowers (2011), these can vary up to a factor of 3.6 (from 250 kg/m^3 for the lightest snow to 900 kg/m^3 for ice). However, in the July period considered above, we are confident that surface conditions did not change, and surface lowering is a reliable proxy for meltwater production at the AWS location.

Figure 13 shows the relative amplitude computed using the surface elevation record as melt proxy, showing that the increase we have attributed to drainage efficiency is also robust under this alternative approach. This includes the period between July 4th and 30th, where no significant changes in surface conditions occurred in the main study area. Although both approaches have uncertainties and flaws, the increase in the relative amplitude we associate to increased efficiency of the drainage system seem to be robust. Due to its overall magnitude and persistence in periods were the density or degree-day factor are unlikely to have changed considerably.

3 Model continuum formulation

The discrete element model of the main text is easy in principle to generalise to a coupled sheet-network model as in Werder et al. (2013). Instead of our conduits S_K, the model represents cavity-like conduits in averaged way as a sheet with thickness h. The 'sheet' formulation of our discrete element model would be

$$-v_p\frac{\partial N}{\partial t}+\frac{\partial h}{\partial t}+\nabla\cdot\mathbf{q}=m \tag{3}$$

$$\frac{\partial h}{\partial t}=u_b(h_r-h)/l_r-c_2h|P_e|^{n-1}P_e \tag{4}$$

$$\mathbf{q}=\kappa\max(h-h_p,0)^\alpha|\nabla\phi|^{\beta-2}\nabla\phi+\kappa_{\mathrm{leak}}\nabla\phi \tag{5}$$

$$\phi=\rho_igs+(\rho_w-\rho_i)gb-N \tag{6}$$

$$P_e(x,y,t)=\int_\Omega G(x,y,x',y')N(x',y',t)\mathrm{d}x'\mathrm{d}y', \tag{7}$$

which, with some minor notational changes, is the same as the Werder et al. (2013) if we put $h_p=0$ and $G(x,y,x',y')=\delta(x-x')\delta(y-y')$. Here v_p, h_r, l_r, c_2, κ, h_p and κ_{leak} are constants equivalent to V_p, h_K, S_{K0}, c_2, c_3, S_{PK} and k_{leak} in the discrete element model, with l_r/n_c representing an averaging length scale for turning the discrete model into its continuum counterpart. In particular, h_p is the percolation cut-off discussed in the main paper, while G is the continuum version of the discrete averaging kernel G_{ijk}, and we require that $G\geq 0$, $\int_\Omega G(x,y,x',y')\mathrm{d}x'\mathrm{d}y'=1$ for all (x,y).

At this point, the need for an averaging term when computing creep closure may still seem vague, beyond the previously stated need to account for discontinuities in N that can evolve once h drops below the percolation cut-off: when such discontinuities arise, we would expect the closure of

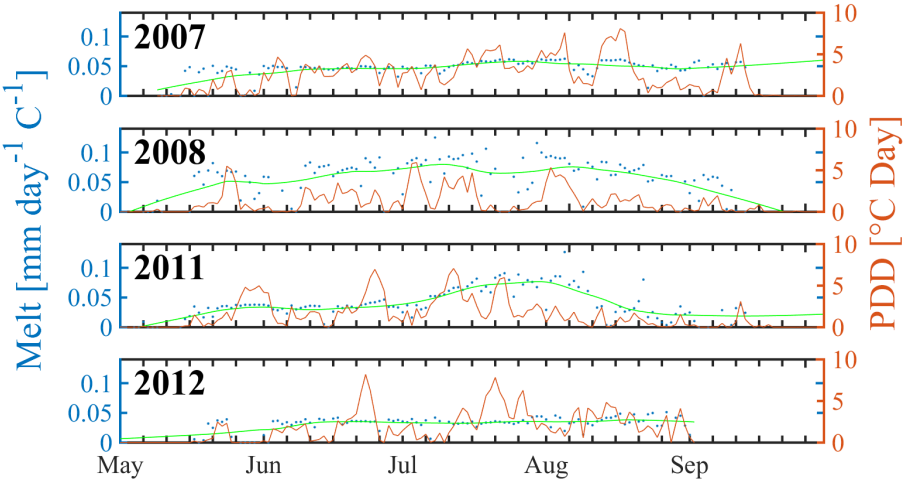

Figure 12. Degree-day factors (blue dots) computed using melt outputs of the model by Wheler and Flowers (2011), and PDD values (orange line) derived from the temperature record. A monthly running median of the degree-day factors is also shown (green line).

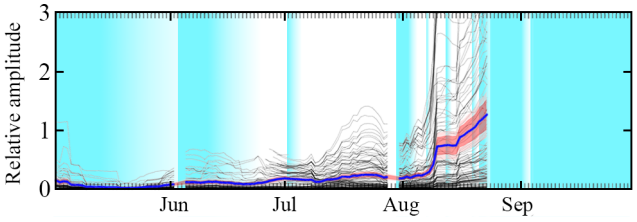

Figure 13. Alternative version of panel c of the Fig. 12c of the main text, using total daily surface lowering as the proxy for the diurnal amplitude of surface meltwater production.

one cavity (that is, the viscous flow of ice around the cavity) to be affected not just by the difference between overburden and water pressure in that single cavity (as is the case in models in which water pressure is the same in all cavities, see Fowler (1986), Schoof (2005) and Gagliardini et al. (2007)), but also by water pressure in other nearby cavities. Effectively, we expect the normal stress transfer effect that we appeal to in order to explain anti-correlated borehole water pressures (see also Murray and Clarke, 1995) to affect cavity creep closure rates. An averaging kernel represents a simple way of attempting to capture this effect, although a more detailed process understanding is certainly a key area for future research.

Practically, the need for some kind of non-local closure is actually easier to understand in the continuum rather than the discrete setting. Take a point (x, y) at which $h < h_p$ and assume that leakage allowed by κ_{leak} is negligible; there is then no water flow at that location. Suppose also that there is no distributed water supply, which would make the persistence of hydraulically isolated patches of bed difficult to maintain. In other words, put $m = 0$. Suppose also that we simply set $P_e = N$. We would obtain a pair of evolution equation for water pressure

$$-v_p \frac{\partial N}{\partial t} + u_b(h_r - h)/l_r - c_2 h|N|^{n-1}N = 0$$

$$\frac{\partial h}{\partial t} = u_b(h_r - h/l_r) - c_2 h|N|^{n-1}N$$

As pointed out by Hoffman et al. (2016), changes in borehole water pressure can now result from temporal variations in ice flow u_b imposed by effective pressure changes elsewhere at the bed. However, in the absence of such imposed sliding velocity variations, the evolution equations for h and N become purely local, and do not couple with the rest of the bed. In particular, if at the point of close-off N was large enough to be causing net closure (so $\partial h/\partial t < 0$ at that point, as required to be entering a closed-off state), it is relatively straightforward to show that close-off will never be reversed, in the sense that h will not rise above h_p again.

The model above excludes the effect of overpressurisation discussed by Schoof et al. (2012), Hewitt et al. (2012) and Tsai and Rice (2010). While overpressurisation undoubtedly contributes to the establishment of hydraulic connections in parts of the season (and we suspect that the spring event, in particular, may be partly driven by overpressurisation) our dateset indicates reconnection events that occur when water pressure is significantly below overburden. In terms of modelling, we are therefore faced with two possibilities: either reconnection is driven purely by ice motion (changes in u_b) or ongoing leakage (so κ_{leak} is not negligible), or changes in water pressure near a given location can drive changes in cavity evolution and connectivity. The averaging kernel G is intended to allow for the latter possibility.

Werder et al. (2013) couple their sheet model to a conduit network model that allows for channelisation. It is straightforward also to generalise that model component to our per-

colation cut-off, by writing

$$\frac{\partial S}{\partial t} = c_1 Q \frac{\partial \phi}{\partial s} + l_c \boldsymbol{q} \cdot \mathbf{t} \frac{\partial \phi}{\partial s} - c_s S |P_e|^{n-1} P_e \tag{8}$$

$$Q = c_3 \max(S - S_{PR}, 0)^{\alpha} \left| \frac{\partial \phi}{\partial s} \right|^{\beta - 2} \frac{\partial \phi}{\partial s} \tag{9}$$

$$\frac{\partial S}{\partial t} + \frac{\partial Q}{\partial s} = \frac{\rho_i}{\rho_w} c_1 Q \frac{\partial \phi}{\partial s} \tag{10}$$

where s is the arc length coordinate along the conduit and $\mathbf{t}$ the unit tangent vector in the direction of increasing s, and all quantities are evaluated at the channel location. S replaces the earlier variable S_R, and S_{PR} is the relevant percolation cut-off. At nodes of the network, there may be additional volume storage and water input as described Werder et al. (2013).

While the simple transcription of the earlier model in Werder et al. (2013) to a percolation cut-off is relatively straightforward, it is not devoid of deeper modelling issues. Defining the closure term P_e non-locally, in particular, makes the identification of (3) as "parabolic" in the variable N questionable: the non-local closure term is not monotone in the usual sense (Ekeland and Temam, 1976), while the diffusion term can vanish on part of the domain. In particular, substituting for $\partial h/\partial t$ in (3), replacing $N = \phi_0 - \phi$ with $\phi_0 = \rho_i g s + (\rho_i - \rho_w) g b$, multiplying by a test function θ and integrating over the domain yields the weak form

$$\int_\Omega v_p \theta \frac{\partial \phi}{\partial t} + \kappa_0 \max(h - h_p, 0)^{\alpha} |\nabla \phi|^{\beta - 2} \nabla \phi \cdot \nabla \theta \, \mathrm{d}\Omega +$$

$$\int_\Omega u_b (h_r - h)/l_r \theta - c_2 h |P_e|^{n-1} P_e \theta - m\theta \, \mathrm{d}\Omega + \int_{\partial\Omega} \boldsymbol{q} \cdot \boldsymbol{n} \, \mathrm{d}\Gamma = 0,$$

where $\boldsymbol{n}$ is the outward-pointing unit normal to the domain. Isolating the non-local closure term as

$$\langle A\phi, \theta \rangle = \int_\Omega -c_2 h |P_e|^{n-1} P_e \theta \, \mathrm{d}\Omega$$

where

$$P_e(x,y,t) = \int_\Omega G(x,y,x',y') \left[\phi_0(x',y') - \phi(x',y',t) \right] \mathrm{d}x' \mathrm{d}y'$$

there appears to be no obvious reason, even with the stipulations that $G \geq 0$, $\int_\Omega G(x,y,x',y') \mathrm{d}x' \mathrm{d}y' = 1$, that we should always have monotonicity in the sense that

$$\langle A\phi - A\theta, \phi - \theta \rangle \geq 0$$

for all functions θ, ϕ.

While this observation may seem a technicality from the modelling perspective, it is relevant to the numerical solution of the problem, the non-local definition of closure has more significant implications when we try to adapt the model for overpressurisation as is done in Schoof et al. (2012) and Hewitt et al. (2012). The formulation in these papers relies on ice being able to separate from the bed when the effective pressure driving the closure term $c_2 h |P_e|^{n-1} P_e$ vanishes; rather than requiring negative effective pressure to enlarge the ice-bed gap, the model then allows the gap evolution to be dictated by the evolution of water depth, identifying the two with each other. At the same time, the extended model of Schoof et al. (2012) and Hewitt et al. (2012) also permits water and ice to separate where water pressure drops to zero. In their model formulation, $P_e = N$ and it is impossible for effective pressure and water pressure to vanish at the same time, which is essential for their model formulation. With a non-locally defined effective pressure P_e, this does become a at least a theoretical possibility: we expect that ice-bed separation occurs when $P_e = 0$, which can in principle occur at the same time as N reaching the value $\rho_i g(s - b)$ required for water pressure to drop to zero; in that case, we could have full ice-bed separation with the gap between the two not filled completely by water, but at least partially by air. In the models of Schoof et al. (2012) and Hewitt et al. (2012), this would however leave the rate of change of the ice-bed gap indeterminate.

This possibility strongly suggests that, at least if we are to model partial flotation of the ice, a more careful approach to non-local closure of the sheet is required, possibly based on a more detailed study of cavity opening and closing in situations where cavities can become closed off from each other and water pressure may differ from cavity to cavity. Such partial flotation may be essential in explaining the formation of an active drainage system in the early melt season, especially if it is possible for drainage connections to close off completely over winter.

References

Ekeland, I. and Temam, R.: Convex Analysis and Variational Problems, North-Holland, Amsterdam, 1976.

Fowler, A.: A sliding law for glaciers of constant viscosity in the presence of subglacial cavitation, Proc. R. Soc. Lond. A, 407, 147–170, 1986.

Gagliardini, O., Cohen, D., Råback, P., and Zwinger, T.: Finite-element modeling of subglacial cavities and related friction law, J. Geophys. Res., 112, https://doi.org/10.1029/2006JF000576, 2007.

Hewitt, I., Schoof, C., and Werder, M.: Flotation and free surface flow in a model for subglacial drainage. Part 2. Channel flow, J. Fluid Mech., 702, 157–187, 2012.

Hoffman, M., Andrews, L., Price, S., Catania, G., Neumann, T., Lüthi, M., Gulley, J., Ryser, C., Hawley, R., and Morriss, B.: Greenland subglacial drainage evolution regulated by weakly connected regions of the bed, Nature Communications, 7, 13903, https://doi.org/10.1038/ncomms13903, 2016.

Kavanaugh, J. and Clarke, G.: Evidence for extreme pressure pulses in the subglacial water system, journal of Glaciology, 46, 9083–9100, 2000.

Murray, T. and Clarke, G.: Black-box modeling of the subglacial water system, journal of Geophysical Research, 100, 10 219–10 230, 1995.

Schoof, C.: The effect of cavitation on glacier sliding, Proceedings of the Royal Society of London A: Mathematical, Physical and Engineering Sciences, 461, 609–627, https://doi.org/10.1098/rspa.2004.1350, http://rspa.royalsocietypublishing.org/content/461/2055/609, 2005.

Schoof, C., Hewitt, I., and Werder, M.: Flotation and free surface flow in a model for subglacial drainage. Part 1. Distributed drainage, J. Fluid Mech., 702, 126–156, 2012.

Tsai, V. and Rice, J.: A model for turbulent hydraulic fracture and application to crack propagation at glacier beds, journal of Geophysical Research: Earth Surface, 115, https://doi.org/10.1029/2009JF001474, f03007, 2010.

Werder, M., Hewitt, I., Schoof, C., and Flowers, G.: Modeling channelized and distributed subglacial drainage in two dimensions, J. Geophys. Res., 118, 2140–2158, 2013.

Wheler, B. and Flowers, G.: Glacier subsurface heat-flux characterizations for energy-balance modelling in the Donjek Range, southwest Yukon, Canada, journal of Glaciology, 57, 121–133, 2011.